PHYSICAL REVIEW FLUIDS **3**, 104801 (2018)

Editors' Suggestion

Numerical investigation of breaking internal solitary waves

Giovanni la Forgia*
Department of Engineering, Roma Tre University, 00146 Rome, Italy
and Institute of Atmospheric Sciences and Climate, National Research Council, 00133 Rome, Italy

Talia Tokyay
Department of Civil Engineering, Middle East Technical University, Ankara 06800, Turkey

Claudia Adduce
Department of Engineering, Roma Tre University, 00146 Rome, Italy

George Constantinescu
Department of Civil and Environmental Engineering, IIHR—Hydroscience and Engineering,
University of Iowa, Iowa City, Iowa 52242, USA

(Received 30 December 2017; published 4 October 2018)

High-resolution three-dimensional large-eddy simulations are used to investigate the effects of internal solitary waves (ISWs) breaking over a sloping boundary. The lock release method is applied in a two-layer stratified fluid system to generate three different breaking mechanisms (i.e., plunging, collapsing, and surging breakers). The different breaking types are investigated in terms of their effects on the dynamics of the ISW and the interaction of the ISW with the sloping boundary. During each breaking event, the pycnocline region entrains fresher water from the upper layer and saltier water from the lower one. The associated increase of the intermediate density layer also induces changes of the pycnocline water density. This process occurs with a velocity that can be evaluated using the bulk entrainment parameter. We show how the intermediate layer features depend on the ISW shoaling and breaking dynamics and we discuss entrainment in breaking ISWs. The instabilities induced by boundary layer separation allow entrainment of saltier water, while the run-up of the gravity current causes the decrease of the intermediate layer mean density. Simultaneously, the entrained water mixes into the pycnocline region. For all cases, the temporal evolution of the instantaneous mixing efficiency is discussed. The plunging breaker case shows the largest amount of mixing, which is mostly induced by rear-edge overturning in the onshore direction. The largest entrainment is observed in the surging breaker case in response to the large gravity current flowing upslope. The paper discusses how the different turbulent instabilities induced by the ISWs breaking affect the time delay between the times when entrainment of patches of salty and fresh water from the neighboring layers occurs and the time the density of the intermediate layers becomes fairly uniform via mixing. We finally point out that the entrainment parameter and the mixing efficiency describe two different effects of the turbulent instabilities occurring in a stratified fluid in terms of changes of the bulk density profile.

DOI: 10.1103/PhysRevFluids.3.104801

---

*giovanni.laforgia@uniroma3.it

2469-990X/2018/3(10)/104801(20)

I. INTRODUCTION

In the ocean, the density profile can be approximated by two layers of uniform density: the lighter well-mixed surface waters, affected by seasonal changes in temperature, and the deep heavier waters [1,2]. Between them, the thin portion of the water column characterized by a sharp change in density is the pycnocline region. This region can be described as a very stable layer which opposes the transfer of mass between the waters it separates. The interaction between the barotropic tide and the bathymetry generates internal tides which induce large-amplitude undulations of the pycnocline. Because of nonlinearities, during their propagation, the internal tides steepen and disperse, generating trains of internal solitary waves (ISWs). Solitary waves preserve their shape and celerity during their motion because of an equilibrium between dispersive and nonlinear effects [3]. The velocity field of an ISW induces water parcel motions (in the same direction as the wave propagation in the upper layer and in the opposite direction in the lower layer), because their paths are composed of open orbits [4]. For this reason, ISWs are able to transport kinetic and thermal energy during their propagation [5].

Internal solitary waves interacting with the continental or near-shore slope can shoal and then break. Shoaling and breaking ISWs induce mixing, which in turn affects the temperature field [6–8] and the spatial distribution of nutrients and oxygen [6,9,10]. Moreover, the shear velocities induced at the bottom cause bed material resuspension and redistribution [11–17].

In recent years, scientific research has focused on analyzing the particular conditions that induce ISW breaking and associated effects. The weakly nonlinear, weakly dispersive Korteweg–de Vries (KdV) equation approximates the shape of shoaling ISWs as a squared hyperbolic secant [18]. The KdV theory is valid for ISW amplitudes of up to 0.4 times the shallow water depth. For larger amplitudes compared to the total water depth, thus in shallow water, the wave structure is significantly different from that predicted by KdV theory and nonanalytical methods must be used to characterize internal wave dynamics. Moreover, it is quite difficult to analyze the ISWs features and their shoaling and breaking processes based on field observations because of the fairly coarse spatial and time resolution of field data [7,8,12,17,19–23]. For these reasons, experimental and numerical studies of shoaling and breaking ISWs have been widely carried out using small-scale idealized domains (see, e.g., [24–26]). Numerous laboratory experiments investigating the interaction of ISWs with a uniform sloped surface have been performed in the past. For example, the study of Kao *et al.* [27] investigated the loss of energy due to breaking ISWs. In another experimental study, Helfrich [28] investigated boluses caused by the shoaling of ISWs. Michallet and Ivey [29] evaluated the energy loss due to mixing induced by shoaling ISWs. Boegman *et al.* [30] classified the observed breaking types as a function of the Iribarren number defined as the ratio between the topographic slope and the square root of the wave slope. The latter is defined as the ratio between the wave amplitude and the wavelength. La Forgia *et al.* [31] investigated the effects of breaking ISWs on the pycnocline thickness. For plunging breakers, they found a nonlinear relation between the Iribarren number and the increase of the pycnocline thickness induced by the wave breaking. Several studies focused on transport due to ISWs breaking on slopes [24–26,28,32]. Helfrich [28] investigated the onshore transport associated with the dense fluid flowing upslope as a gravity current after the breaking event takes place [33]. Nakayama and Imberger [32] and Nakayama *et al.* [24] quantified transport by means of a time-averaged residual circulation: Their laboratory experiments and numerical simulations showed that transport occurs onshore in the upper layer and offshore in the lower layer. Arthur and Fringer [26] distinguished an onshore transport due to the upslope flow of the denser fluid and an offshore transport induced by an intrusion of mixed fluid propagating upstream. As generally observed in the coastal regions of oceans, these intrusions resemble intermediate nepheloid layers, inducing offshore transport of benthic material into the interior of the water column [34].

Formation and propagation of internal bores in two-layer stratified environments were studied based on eddy resolving simulations by Borden *et al.* [35,36]. Shoaling and breaking internal waves on slopes have been extensively investigated numerically, both at field scales [8,37–39] and

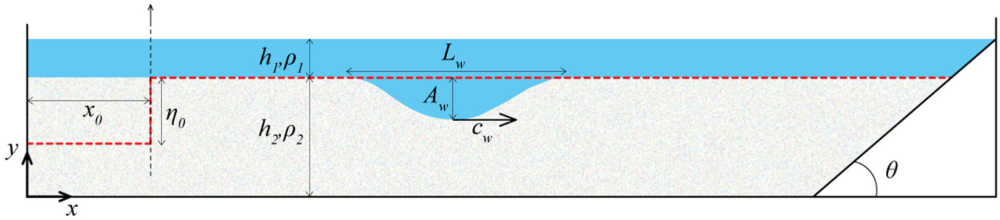

FIG. 1. Sketch of the domain used to study breaking ISWs on slopes. The dashed line represents the initial pycnocline position in the two layer-stratified fluid. The black dashed vertical line shows the initial position of the lock gate.

at laboratory scales [40–43]. Moreover, several high-resolution, three-dimensional (3D) numerical studies have examined turbulence and mixing during internal wave breaking on slopes. One can mention the direct numerical simulations (DNSs) of Gayen and Sarkar [44] and Arthur and Fringer [26,45] and the large-eddy simulations (LESs) of Gayen and Sarkar [46] among others. Each ISW breaking mechanism is characterized by a peculiar dynamics and consequently different effects in terms of mixing, entrainment, and the shear stresses induced over the sloped surface. During the wave shoaling, the rear edge of the wave steepens and the denser fluid confined between the leading edge and the incline moves downward. Depending on the ISW geometric features and the slope inclination, the ISW shoaling over the sloping boundary develops differently [31]. For plunging breakers, the steepening of the trailing edge is followed by a quick overturning in the onshore direction, which entrains denser water and induces strong local mixing [47]. For collapsing breakers, the rear edge steepening occurs slowly and it does not involve any observable instability. At the same time, the dense water confined between the wave and the slope leaves its original position with a fast downward motion in the adverse pressure gradient region. The consequent decrease of downslope velocities induces boundary layer separation. As a result, a turbulent separated bolus forms that quickly dissipates [43]. Then, part of the incident wave is reflected and a gravity current composed of the denser fluid flows up the slope, until hydrostatic conditions are reestablished. In the case of surging breakers, the ISWs are not subject to any observable large-scale instability during the shoaling until the wave trough reaches the sloping bottom. The wave is not completely reflected because a gravity current composed of denser fluid moves up the slope and strongly amplifies mixing [47].

Instabilities induced by ISWs breaking cause mixing and entrainment of both fresh and salty water into the pycnocline region. The entrainment parameter is used to quantify the normalized velocity of water discharge per unit area through the pycnocline boundaries, defined as the 2% and 98% isopycnal surfaces. A similar approach was adopted to study the entrainment of ambient fluid in gravity currents [48–52]. Although ISWs have been widely studied in the past, the contribution of this work is the investigation of entrainment in breaking ISWs. The present study uses fully 3D LES to investigate ISWs shoaling and breaking effects in terms of mixing and entrainment. Because each breaking mechanism is characterized by different dynamics, our goal is to use the 3D flow fields available from highly resolved LES to qualitatively and quantitatively describe the effects induced by the different ISWs breaking types. Section II describes the procedure adopted to generate a certain type of breaker, as well as the main parameters of the experiments that are used for validation of the numerical method. Section III describes the numerical model, previous validation studies, boundary conditions, and simulation setup. Section IV investigates entrainment processes. In Sec. V we discuss the ISW energetics and evaluate irreversible mixing. Section VI discusses the significance of the main results and provides some conclusions.

II. INTERNAL SOLITARY-WAVE GENERATION AND RELATED EXPERIMENTS

Laboratory experiments were performed at the Hydraulics Laboratory of Roma Tre University in a 3.0-m-long, 0.2-m-wide, and 0.3-m-deep Perspex tank (Fig. 1). The ISW was generated using a standard lock-release setup [27]. A thin, vertical, removable Perspex gate was used to divide the regions containing lock fluid, on the left-hand side of the tank, and ambient fluid. A stratified two-layer distribution containing fresh water in the upper layer (h_1) and salty water in the lower one (h_2) was used to the right of the lock gate before the start of the experiment. The density difference for the experiments performed ranges between 29.5 and 30.6 kg/m^3. The Boussinesq parameter values (0.0295–0.0306) are typical of those ($\sim$0.03) observed in coastal ocean regions where solitary waves are forming [53]. The Boussinesq parameter is defined as the ratio of the density difference between the two layers and a reference density. To produce this initial density stratification, the entire domain was filled with a solution of sodium chloride generating the lower layer of uniform density ρ_2. A density meter (Anton Paar DMA 4100M) was used to measure the density of the saline mixture. Its measurement accuracy was 0.1 kg/m^3. Fresh water of uniform density $\rho_1 < \rho_2$ dyed by a controlled quantity of Methylthioninium chloride was then poured slowly into a funnel inlaid in a sponge float placed over the free surface. Later, the vertical gate was inserted at a distance x_0 from the left wall of the tank. The bottom of the lock gate did not touch the channel bottom but penetrated beneath the bottom of the layer containing lighter fluid in the lock region. The addition of fresh water of uniform density ρ_1 on the free surface of the lock induced the formation of a displacement η_0 between the pycnoclines of the two regions. During this phase, a known volume of brine water flowed below the gate, reestablishing the hydrostatic equilibrium. The thickness of the layer containing salty water was $h_1 + h_2$ on the left of the lock gate and h_1 on its right (see the dashed line in Fig. 1 that visualizes the interface between the heavier and light fluid before the gate removal). The gate removal results in a gravity collapse that induces the generation of an ISW of depression propagating toward the sloping boundary. The incline makes an angle θ with the horizontal. At a fixed distance from the front wall of the tank, a CCD camera with a frequency of 25 Hz and a spatial resolution of 1024 × 668 pixels was placed to record the evolution of the ISW in each experiment. Each pixel had a resolution of about 3×3 mm^2. Using image analysis, the pycnocline thickness and the pycnocline position were inferred. For each generated ISW, the wave amplitude A_w, the wavelength L_w, and the wave surface S_w (Fig. 1) were measured. Additionally, the wave celerity c_w (the first derivative of the trough's position) was estimated. The characteristic wavelength λ_w [29] was estimated from the relation

$$\lambda_w = \frac{1}{A_w} \int_{-\infty}^{+\infty} \eta(x) dx = \frac{S_w}{A_w}, \tag{1}$$

where $\eta(x)$ is the pycnocline vertical displacement compared to its original position.

Our goal was to generate well-defined ISWs in terms of their geometric features such that three different breaking mechanisms are observed in a series of experiments conducted with different values of θ or, equivalently, of the topographic slope $s_b = \tan(\theta)$. The breaking mechanisms are generally classified based on the internal Iribarren number [30,31,43,47]. This dimensionless parameter is defined as

$$I_r = \frac{s_b}{\sqrt{\frac{A_w}{\lambda_w}}}. \tag{2}$$

La Forgia *et al.* [31] developed empirical relations between the experimental setting parameters before the lock gate release (x_0, η_0, h_1, and h_2) and the wave geometric features (A_w and λ_w). They observed plunging breakers for $I_r < 1$, collapsing breakers for $I_r = 1$–1.5, and surging breakers for $I_r > 1.5$. The ISW experiments reported in this study were conducted in the same Perspex tank used by La Forgia *et al.* [31]. Table I shows the parameters in the three experiments (cases 1–3) discussed in this study for which a plunging, a collapsing, and a surging breaker were observed, respectively. In agreement with previous experimental studies [30,31,47], the slopes used in the laboratory experiments are selected in order to generate well-defined plunging, collapsing, and surging breaking mechanisms.

TABLE I. Main parameters of the internal solitary wave cases. The variables in the table indicate the breaker type (plunging P, collapsing C, or surging S), the densities of the upper and lower layers ρ_1 and ρ_2, respectively, the lock length x_0, the pycnocline displacement η_0, the depth of the layers in the ambient fluid region h_1 and h_2, the wave amplitude A_w, the characteristic wavelength λ_w, the wave celerity c_w, the wave surface S_w, the topographic slope s_b, and the internal Iribarren number I_r.

Case	Type	ρ_1 (kg/m^3)	ρ_2 (kg/m^3)	x_0 (cm)	η_0 (cm)	h_1 (cm)	h_2 (cm)	A_w (cm)	λ_w (cm)	c_w (cm/s)	s_b	I_r
1	P	1001.7	1031.7	10.0	18.0	1.2	19.8	3.9	24.8	11.6	0.284	0.7
1	C	1001.0	1031.6	15.0	9.2	5.0	23.0	3.3	42.4	12.8	0.366	1.3
1	S	1001.0	1030.5	15.0	13.5	3.3	16.7	5.3	41.1	15.7	0.953	2.6

III. NUMERICAL MODEL, SIMULATION SETUP, AND VALIDATION

The numerical model was previously applied to study bottom propagating and intrusion lock-exchange gravity currents [54–57] and internal bores [35]. The Boussinesq approximation is employed to account for stratification effects. Here we only briefly describe the main features of the numerical algorithm. The governing Navier-Stokes and density transport equations are solved in nondimensional form with the channel height $H = h_1 + h_2$ as the spatial scale and the buoyancy velocity $u_b = (g'H)^{0.5}$ as the velocity scale. The reduced gravity is $g' = g\frac{\rho_2-\rho_1}{\rho_2}$, where g is the gravitational acceleration. The dimensionless density field is defined as

$$\rho^*(x, y, z, t) = \frac{\rho(x, y, z, t) - \rho_1}{\rho_2 - \rho_1}. \tag{3}$$

The finite-volume viscous solver [58] advances the Navier-Stokes equations in time using a semi-implicit iterative method. The pressure Poisson equation is solved using multiple grids. The conservative form of the nondimensional Navier-Stokes equations is integrated on nonuniform Cartesian meshes. All operators in the momentum and pressure equations are discretized using second-order central schemes. The algorithm is second order in time. Discrete energy conservation ensures robustness at relatively high Reynolds numbers despite using strictly nondissipative (central) schemes to discretize the Navier-Stokes equations. A standard advection-diffusion equation is solved for the nondimensional density. The quadratic upstream interpolation for convective kinematics scheme is used to discretize the advective term in the equation for ρ^*. The FORTRAN 90 parallel code uses a message passing interface. The two parameters in the nondimensional governing equations are the channel Reynolds number $\mathrm{Re} = u_b H/\nu$ and the molecular Schmidt number $\mathrm{Sc} = \nu/\kappa$, where ν is the molecular viscosity and κ is the molecular diffusivity. The subgrid-scale viscosity and the subgrid-scale diffusivity in the filtered nondimensional momentum and density equations are calculated using the dynamic Smagorinsky model [58] based on the resolved velocity and density fields at each time instant. As opposed to the classical constant-coefficient Smagorinsky model, the dynamic version does not require any near-wall corrections or corrections to account for stratification effects [59]. It also correctly predicts zero values of the subgrid-scale viscosity and diffusivity in regions where the flow is nonturbulent even in the presence of mean shear or where the flow is relaminarizing, which is particularly important for the types of flows that are investigated in the present study. Also the values of the subgrid-scale viscosity and subgrid-scale diffusivity in the instantaneous flow fields are significantly lower than those predicted by the constant coefficient Smagorinsky model. For the relatively fine mesh used in the present simulations and relatively low physical Reynolds number, the maximum values of the eddy viscosity and eddy diffusivity in the instantaneous flow fields were of the order of 10 times the corresponding molecular values. At most grid points situated inside the ISW region and around it where the flow is turbulent, the instantaneous subgrid-scale viscosity and diffusivity values were comparable to or lower than the molecular viscosity and diffusivity, respectively. This means that the present simulations resolve most of the energetically important eddies in the flow and the subgrid-scale model has a small effect on the dynamics of these eddies other than providing the minimum dissipation that keeps the simulation stable.

The LES-DNS code was validated for several relevant types of flows relevant for the present investigation. Ooi *et al.* [54] discussed validation results for intrusion currents propagating in a two-layer stratified environment. Tokyay and Constantinescu [60] and Steenhauer *et al.* [61] discussed validation for a gravity current interacting with a large triangular obstacle and lock-exchange currents propagating over a sloped surface, a setup that is directly relevant for the present study once the ISW starts interacting with the sloped surface. Borden *et al.* [35] investigated the propagation of internal bores generated in lock-exchange configurations. All these studies contain a detailed comparison with experimental data and shallow water theory. The same code was also used to calculate mixing and mixing efficiency in stratified turbulence. Sommer *et al.* [62] reported such a study conducted for bacteria-induced mixing in a stratified lake environment. The flow dynamics, flow velocities within the convection cells forming inside the bacteria layer, the dissipation levels, and the mixing efficiency were found to be close to values estimated based on field experiments conducted in a lake with similar stratification and flow conditions.

The geometrical setup of the simulations in a horizontal-vertical plane x-y is shown in Fig. 1. A zero flow velocity field is imposed in the domain at the time when the lock gate is released ($t = 0$). All the solid channel boundaries, including the inclined surface, were treated as no-slip surfaces. Periodic boundary conditions were applied for all variables in the spanwise direction.

The top boundary (free surface of the tank) was treated as a shear-free slip surface with zero normal velocity. Before the lock gate was released at $t = 0$, the nondimensional density was set up as $\rho^* = 1$ in the region containing the saltier fluid and $\rho^* = 0$ in the remaining part of the tank containing ambient lighter fluid (see the red dashed line in Fig. 1). A small 3D disturbance was imposed on the initial density field in the regions delimitating the saltier and ambient fluids. The surface-normal concentration gradient was set to zero at all no-slip and free-slip boundaries. The molecular Schmidt number was equal to 100. Ooi *et al.* [63] investigated the effect of the molecular Schmidt number on the propagation and mixing of bottom propagation gravity currents using the same LES code. They found that the main variables characterizing the evolution of the turbulent current were close to being independent of the value of the molecular Schmidt number for $1 < \mathrm{Sc} < 100$. These results are also fully consistent with similar conclusions reached based on DNS by Necker *et al.* [64] and Cantero *et al.* [65], who found that the value of the Schmidt number does not significantly alter the generality of the results as long as it is of order one or larger. In all the simulations the grid contained over 70×10^6 nodes with 64 grid points in the spanwise direction. The grid spacing in the spanwise direction was about $0.008H$, while the grid spacing in the vertical and streamwise directions was close to $0.0035H$. At most locations the boundary layer on the inclined surface was resolved with at least five points in the wall-normal direction. This resolution is comparable to the one used by Steenhauer *et al.* [61] to study the propagation of lock-exchange gravity currents over inclined surfaces at comparable physical Reynolds numbers for which experimental data were available for validation of the numerical predictions. Simulations were run with a time step of $0.002H/u_b$. A grid dependence study was conducted for case 1. It confirmed that the mesh density used in the present simulations was sufficient for the solutions to be considered grid independent. In the simulations, the flow is homogeneous in the spanwise direction. This allows defining the mean (spanwise-averaged) variables at any moment in time. The spanwise-averaged values are denoted as $\langle\,\rangle$. The wave Reynolds number Re_w is evaluated as in [43],

$$\mathrm{Re}_w = \frac{A_w c_0}{\nu}, \tag{4}$$

where the linear phase speed c_0 is defined as in [47],

$$c_0 = \sqrt{g' \frac{h_1 h_2}{h_1 + h_2}}. \tag{5}$$

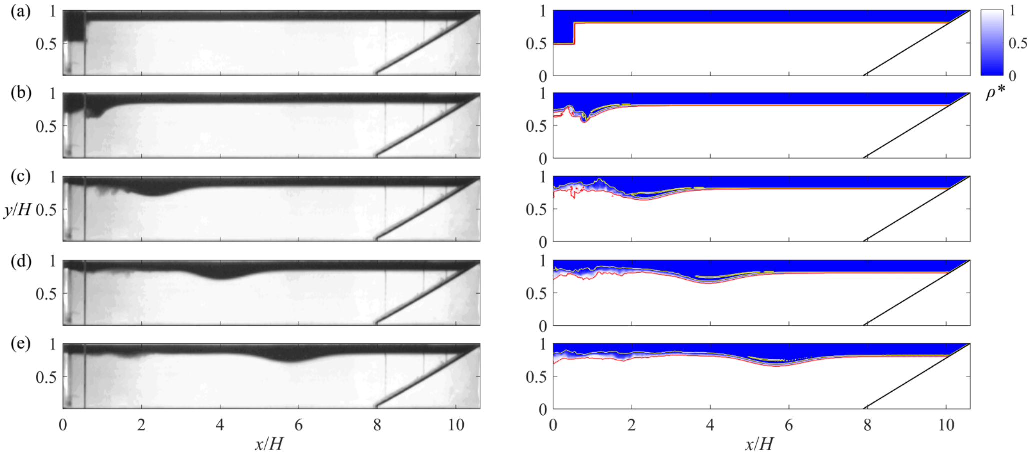

FIG. 2. Snapshots in time visualizing the heavier fluid in the experiments (on the left) and the nondimensional density fields obtained by numerical simulation (on the right) for the collapsing case (case 2) (a) after the experimental or numerical initial setting ($t'/T = -5.1$), (b) a short time after the gate is removed ($t'/T = -4.51$), (c) after the ISW formation ($t'/T = -3.43$), (d) during the ISW propagation toward the sloping boundary ($t'/T = -2.34$), and (e) before the interaction of the ISW with the sloping boundary ($t'/T = -1.23$). Yellow and red lines visualize the 2% and 98% isopycnal surfaces, respectively.

The inferred wave Reynolds numbers for the three cases are $\mathrm{Re}_w = 2.25 \times 10^3$ (case 1), $\mathrm{Re}_w = 3.66 \times 10^3$ (case 2), and $\mathrm{Re}_w = 4.91 \times 10^3$ (case 3). To interpret more easily the differences among the three cases, Sec. VI analyzes the relevant variables in nondimensional form. The nondimensional time scale is $T = \lambda_w/c_w$. The time scale T is 2.14, 3.31, and 2.62 s in cases 1, 2, and 3, respectively. Given that the focus of the present study is on the interaction of the ISW with the sloped surface and that the length of the tank has a small effect on the ISW characteristics before it approaches the sloped surface, the time in each simulation (t') is specified with respect to the time (t_0) at which the horizontal velocity in the upper layer starts to decrease because of the presence of the sloping boundary. In nondimensional form, $t'/T = (t - t_0)/T$, where t is measured with respect to the time at which the lock gate is removed ($t/T = 0$).

We assessed the reliability of the numerical model by comparing the results of the numerical simulations with those obtained from laboratory experiments performed as part of the present research. For all three cases, the numerical simulations predicted the formation of an ISW with geometric and kinematic features (i.e., amplitude, wavelength, and celerity) very close to those observed in the corresponding experiments. For brevity, only numerical results for case 2, in which a collapsing breaking mechanism is observed, are compared in Figs. 2 and 3 with experimental visualizations. For the corresponding time steps, the right-hand side of Figs. 2 and 3 shows the (nondimensional) density field $\langle \rho^* \rangle$ predicted by the numerical simulation at relevant times after the formation of the ISW. In the experiment (left-hand side of Figs. 2 and 3), the dye introduced inside the upper lighter layer allows one to directly observe the spatial and temporal evolutions of the pycnocline. The frames in Fig. 2 visualize the ISW generated by the lock release at $t'/T = -5.1$ or $t/T = 0$ [Fig. 2(a)]. The most obvious discrepancy between the experiments and the way the simulation was conducted is the presence of a thin Perspex gate introduced during the filling phase inside the tank to generate a different stratification between the lock and the ambient fluid regions. Moreover, the gate removal induces a transfer of vertical shear stress to the fluid parcels in direct contact with it. However, given the small thickness of the Perspex gate (4 mm) and the low gate removal rate, the induced disturbances are fairly limited and confined. Figure 2(b) confirms that, immediately after the gate removal, the simulated density field nearby the lock region is in good

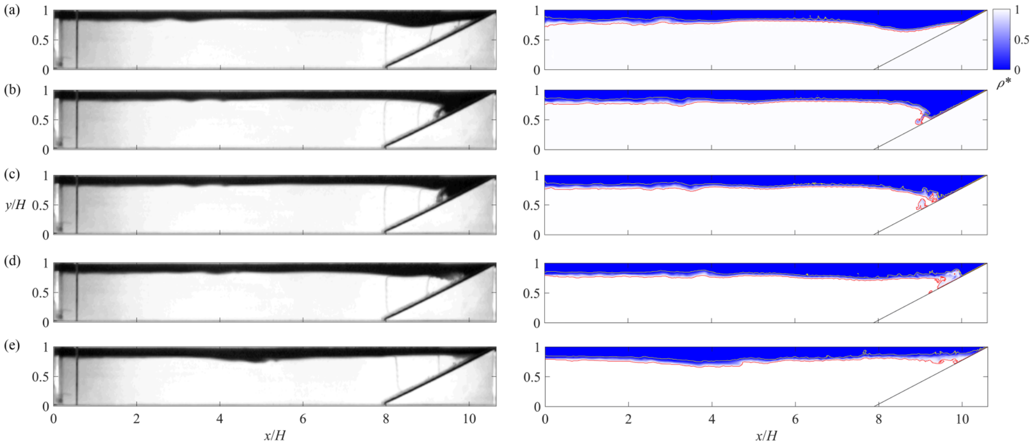

FIG. 3. Snapshots in time visualizing the heavier fluid in the experiments (on the left) and the nondimensional density fields obtained by numerical simulation (on the right) for the collapsing case (case 2) (a) at the time at which the ISW starts interacting with the sloping boundary and the horizontal velocity in the upper layer starts to decrease because of the presence of the sloping boundary ($t'/T = 0$); (b) during the bolus generation, point A in the following figures ($t'/T = 1.7$); (c) at a time when mixing induced by the bolus is significant, point B in the following figures ($t'/T = 2.05$); (d) after the gravity current running up the slope forms, point C in the following figures ($t'/T = 2.96$); and (e) at the time the gravity current reaches the end of the slope, point D in the following figures ($t'/T = 5.59$). Yellow and red lines characterized the 2% and 98% isopycnal surfaces, respectively.

agreement with the spatial distribution of dye observed experimentally at the same time. At time $t'/T = -4.51$ the lighter fluid initially placed inside the lock region begins to assume the typical shape of a solitary wave [Fig. 2(c)] and propagates while preserving its shape and celerity as it approaches the sloping boundary [Fig. 2(d)]. In both experiment and simulation several bores follow the internal wave, as shown in Fig. 2(c). The bores are comparable in terms of their size and location. This proves again that the disturbance induced by the Perspex gate removal during the laboratory experiment can be considered negligible. Figure 3 visualizes the ISW once it starts interacting with the sloping boundary. The numerical model captures very well the main geometric features of the ISW approaching the inclined surface [Fig. 3(a)]. The collapsing breaking mechanism involves the formation of a bolus characterized by a counterclockwise vortex, which is clearly visible over the inclined surface [31]. Both the location of this instability and its geometric features are well captured by the numerical simulation [Figs. 3(b) and 3(c)]. The wave breaking induces the generation of a gravity current containing heavier fluid running up the inclined surface [Fig. 3(d)], while the approaching ISW is partially reflected [Fig. 3(e)].

To provide a more in depth comparison of the experimental and the numerical flow evolution results in case 2, the temporal evolution of the grayscale field from the experimental visualization and the normalized density field from the simulation are compared in a horizontal plane [Figs. 4(a) and 4(b)] and in a vertical one [Figs. 4(c) and 4(d)]. The strips of dark color in Figs. 4(a) and 4(b) represent a portion of the ISW underlying the horizontal plane placed at $y/H = 0.74$ from the bottom. The thickness and inclination of the two strips are about the same in the experiment and simulation, which is consistent with the good prediction of the ISW size and celerity by the simulation. The breaking of the ISW generates a reflected ISW that is smaller compared to the incident one. This is why the reflected wave is occasionally visible for $t'/T > 1$ at times when it intersects the reference horizontal plane. The reflated waves assume comparable features, for $t'/T > 2.5$ [Figs. 4(c) and 4(d)].

For cases 1 and 3, Fig. 5 shows the nondimensional density fields predicted by the numerical simulations as the ISWs generated by the lock release approach the inclined surface and starts

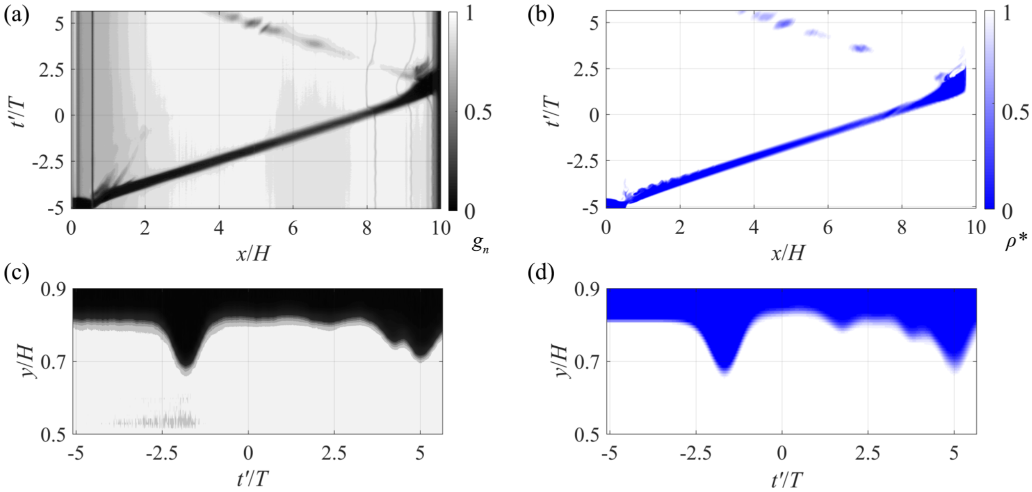

FIG. 4. Case 2 experiment and numerical simulation snapshot with the field of view showing the entire domain. (a) Experimental normalized grayscale field g_n and (b) numerically predicted dimensionless density field $\langle \rho^* \rangle$ in a horizontal plane (x/H-t'/T) situated at fixed depth ($y/H = 0.74$) from the bottom. (c) Normalized grayscale field and (d) numerically predicted dimensionless density field in the vertical plane (t'/T-y/H) at the middle of the domain ($x/H = 5.35$).

interacting with it. The steepening of the trailing edge of the wave for case 1 [Figs. 5(a)–5(e)], the formation of a bolus over the sloping boundary for case 2 [Figs. 3(a)–3(e)], and the formation of

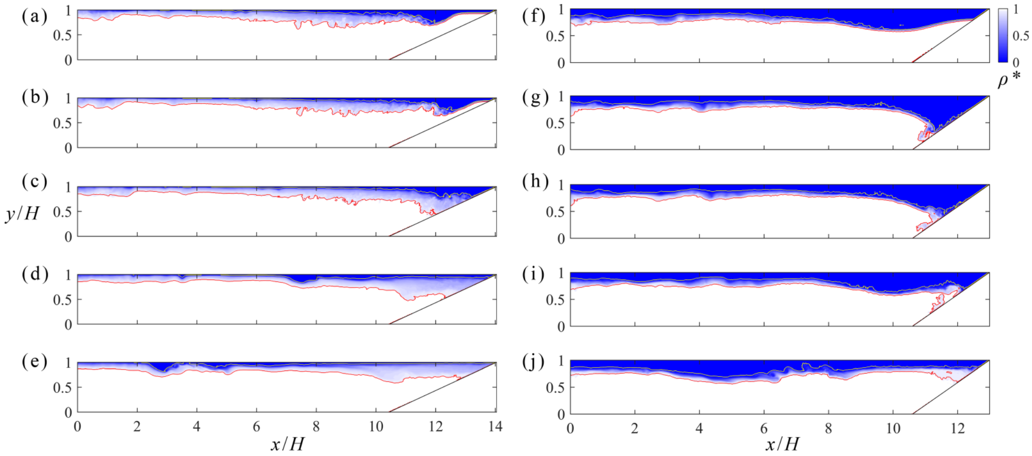

FIG. 5. Nondimensional density fields predicted by numerical simulation for (a)–(e) the plunging case (case 1) and (f)–(j) the surging case (case 3). Shown for the plunging breaker are (a) the wave approaching the slope ($t'/T = 0$); (b) steepening of the trailing edge ($t'/T = 1.03$); (c) mixing induced by the trailing edge overturning, point E in the following figures ($t'/T = 2.46$); (d) gravity current flowing upslope, point F in the following figures ($t'/T = 7.44$); and (e) the gravity current stopping ($t'/T = 13.48$). Shown for the surging breaker are (f) the wave approaching the slope ($t'/T = 0$); (g) small instability for boundary layer separation, point G in the following figures ($t'/T = 1.17$); (h) formation of the gravity current ($t'/T = 1.84$); (i) the gravity current flowing upslope, point H in the following figures ($t'/T = 2.25$); and (j) the gravity current stopping ($t'/T = 3.42$).

a gravity current flowing up the incline for case 3 [Figs. 5(f)–5(j)] represent the main events that characterize the breaking mechanism in the plunging, collapsing, and surging cases, respectively.

IV. ENTRAINMENT IN INTERNAL SOLITARY WAVES

During the ISW generation phase, the pycnocline region entrains both fresh and salty water, increasing its volume. Once the lock gate is released, the initial potential energy is converted into kinetic energy and mixing occurs between the upper layer containing lighter fluid and the lower layer containing heavier fluid. The fresh water entrainment velocity can be estimated as the fresh water discharge per unit area crossing the interface between the two fluids defined by the isodensity level $\langle\rho^*\rangle = 0.02$ in the vertical x-y plane.

This procedure is similar to the one used in Refs. [48,49,52,66–68]. The salty water entrainment velocity is estimated in a similar way using the water discharge per unit area crossing the interface defined by the isodensity level $\langle\rho^*\rangle = 0.98$ in the vertical x-y plane. Figure 5(a) shows the $\langle\rho^*\rangle = 0.02$ and $\langle\rho^*\rangle = 0.98$ isodensity levels as the ISW is approaching the inclined surface in case 2. The arrows perpendicular to the isodensity surfaces identify the direction of the entrainment discharge. We define the intermediate density layer (or pycnocline water) as the region enclosed by these two isodensity levels. The water discharge per unit area crossing these interfaces represents entrainment into the pycnocline water. It can be described by the temporal variation of the intermediate density layer region volume enclosed between the two isodensity levels in the vertical x-y plane.

If at $t = t_0$ ($t'/T = 0$) the initial volume of the pycnocline water is Vm_0, at a successive time $t_i = t_0 + \Delta t_i$ the intermediate density layer has a larger volume $Vm_t = Vm_0 + \Delta V_i$. The change in volume ΔV_i can be estimated as $\Delta V_i = (A_t - A_0)d$, where d is the spanwise dimension of the domain, A_t is the area enclosed between the isodensity levels in the vertical x-y plane at time t_i, and A_0 is the initial area of the pycnocline water at $t = t_0$. A bulk entrainment discharge can be calculated at each time:

$$Q_{ei} = \Delta V_i/\Delta t_i. \tag{6}$$

Then one can define a bulk entrainment velocity

$$W_{ei} = Q_{ei}/S_i, \tag{7}$$

where the interface S_i is obtained as the sum of the isodensity surfaces defining the boundaries of the intermediate density layer. The bulk entrainment parameter EP is a dimensionless number obtained by dividing the bulk entrainment velocity by the ISW celerity

$$\mathrm{EP}_i = W_{ei}/c_w. \tag{8}$$

For each case, the temporal variations of the nondimensional pycnocline water volume Vm/Vm_0 and averaged density $\rho^* - \rho_0^*$ are plotted in Figs. 6(b) and 6(c), respectively. The index 0 is used to denote the values of these variables at $t = t_0$.

Before the ISW reaches the inclined surface (initial phase, $t'/T < 2$), the intermediate density layer volume increases with time at an approximately constant rate in all three cases [Fig. 6(b)]. By contrast, the averaged density does not show a similar variation in the three cases for $t'/T < 2$ [Fig. 6(c)]. After this initial phase, the temporal variations of the pycnocline water volume is a function of the breaking dynamics of the ISW. For the collapsing and the surging cases, the pycnocline water volume continues to increase with about the same initial rate [Fig. 6(a)]. Meanwhile, a much smaller rate of increase of the pycnocline water volume with time is observed in the plunging case for $t'/T > 2$ [Fig. 6(a)]. This is due to the slow decrease of the mean density of the mixing layer [Fig. 6(b)]. The temporal variation of the averaged density is nonmonotonic for all three cases. For the collapsing and the surging cases, $\rho^* - \rho_0^*$ first increases until $t'/T = 3$ and then it starts decreasing in a nonmonotonic way [Fig. 6(b)]. The nonmonotonic decay of $\rho^* - \rho_0^*$ is observed starting immediately after the end of the initial phase in the plunging case. Depending on the breaking dynamics, the changes of the pycnocline water volume and averaged density are

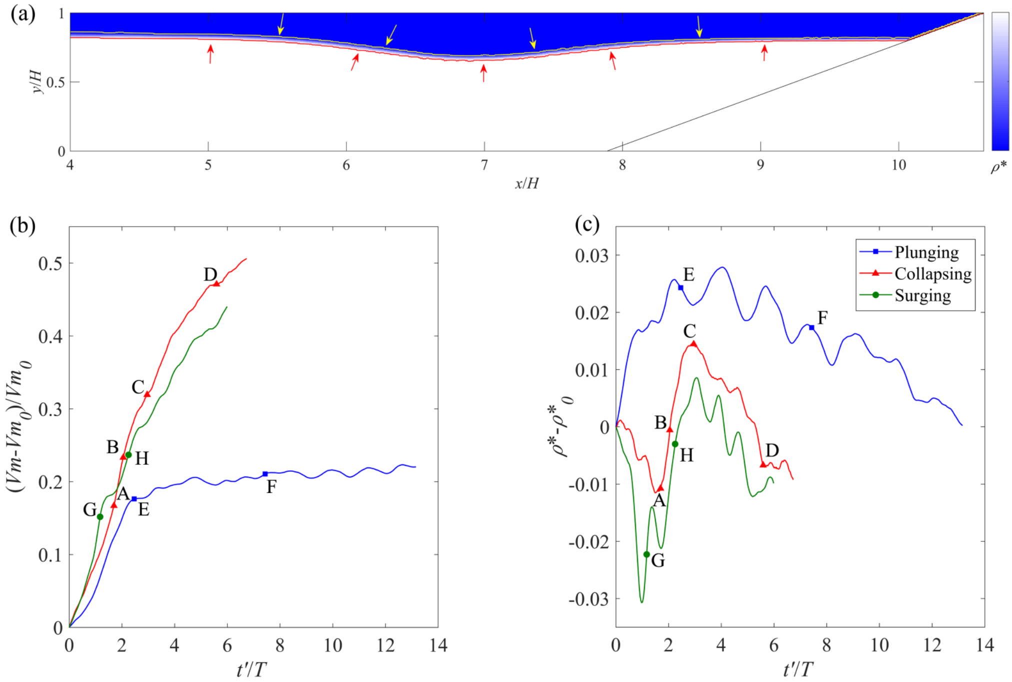

FIG. 6. Analysis of the entrainment process. (a) Case 2, nondimensional density. The arrows identify the direction of the entrainment which occurs perpendicularly to the 2% and 98% isopycnal surfaces (yellow and red lines, respectively). Also shown are the temporal evolution of (b) the dimensionless volume and (c) the averaged density of the pycnocline water. Results are shown for case 1, the plunging breaker (solid lines); case 2, the collapsing breaker (dashed lines); and case 3, the surging breaker (dash-dotted lines). Points *A*–*H* are defined in Figs. 3 and 5.

affected by the entrainment of both fresh and salty water. The physical processes affecting the intermediate density layer evolution can be described by considering the temporal evolution of the bulk entrainment parameter. In particular, one can distinguish between the global bulk entrainment parameter of the pycnocline water (black lines in Fig. 7) and the bulk entrainment parameter evaluated by considering the $\langle\rho^*\rangle = 0.02$ and 0.98 isopycnal surfaces. The former characterizes the entrainment of the fresh water into the salty water (green lines in Fig. 7), while the latter characterizes the entrainment of the salty water into the fresh water (red dashed lines in Fig. 7). As the collapsing breaker approaches the inclined surface in case 2, it modifies its shape without developing any visible instability [Fig. 3(a)]. Its trailing edge steepens, while its leading edge tends to assume the same slope as the incline. As this happens, the wave partially dissipates. The pycnocline water increases its volume by entraining mostly fresh water. This is the main reason why its mean density decreases for small t'/T [e.g., until point A in Figs. 6(b), 6(c), and 7(a)]. As the ISW starts breaking, a bolus characterized by a counterclockwise motion forms and then dissipates fairly rapidly [Figs. 3(b) and 3(c)]. This event induces a sudden change of the bulk entrainment parameter due to the increase of the brine water discharge into the pycnocline water, which increases its density [see the time interval between points A and B in Figs. 6(b), 6(c), and 7(a)]. The generation of a gravity current flowing up the inclined surface is consistent with the counterclockwise direction of the vortex generated by the interaction of the IBW with the inclined surface [see Figs. 3(d) and 3(e) and point C in Figs. 6(b), 6(c), and 7(a)]. The gravity current propagates upslope, interacting with the upper layer containing fresh water. As a result, the gravity current entrains lighter water [see the time interval between points C and D in Figs. 6(b), 6(c), and 7(a)], which explains the decrease of the pycnocline water averaged density. The disappearance of a well-defined gravity

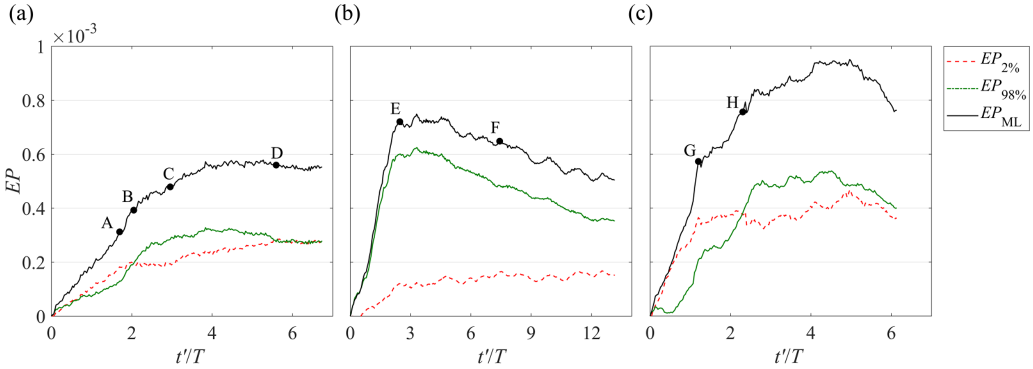

FIG. 7. Temporal variation of bulk entrainment parameter for (a) the collapsing case, (b) the plunging case, and (c) the surging case. The dashed lines show the EP obtained by using the 2% isopycnal surface (entrainment of fresh water), the green solid lines show the EP obtained by using the 98% isopycnal surface (entrainment of salty water), and the black solid lines show the EP obtained by using both the 2% and 98% isopycnal surfaces (entrainment of the fresh water and salty water into the intermediate density layer). Points *A*–*H* are defined in Figs. 3 and 5.

current marks the end of the breaking event. At larger times, the incident wave is partially reflected and the pycnocline water density becomes approximately constant [see the time interval after point *D* in Fig. 6(c)].

For the plunging breaker case, the interaction of the ISW with the sloping boundary [case 1 results in Figs. 5(a)–5(c)] results in the steepening of the rear edge of the wave and its subsequent overturning in the onshore direction [31]. This induces the formation of a clockwise rotating patch of heavier fluid due to the Rayleigh-Taylor instability which causes entrainment of the lower-layer salty water [43]. During the initial stages, increases of the pycnocline water volume and density are observed. They are due to entrainment of salty water into the intermediate density layer [see the time interval before point *E* in Figs. 6(b), 6(c), and 7(b) for case 1]. The rotating patch of fluid slowly dissipates as it entrains less and less brine water. At the same time, as for the collapsing case, a gravity current forms and flows upslope [case 1 in Fig. 5(c)], entraining lighter water into the intermediate density layer [case 1 in Figs. 5(d) and 5(e)]. Consequently, a decrease of the pycnocline water mean density is observed due to a fresh water entrainment [see the time interval after point *E* in Figs. 6(b), 6(c), and 7(b)].

For the surging breaker case, the ISW dynamics is comparable to that observed in the collapsing case. As the wave interacts with the sloping boundary, it changes its shape and partially dissipates as it entrains fresh water [$t'/T < 0.5$ in Figs. 6(b), 6(c), and 7(c)]. When the wave trough reaches its lowest position over the sloped surface, boundary layer separation occurs, inducing the formation of a bolus [case 3 in Fig. 5(g)] characterized by a counterclockwise motion. It quickly dissipates causing mixing. Eventually the bolus evolves into a gravity currentlike flow that advects fresh water upslope [case 3 in Figs. 5(h)–5(i)]. This induces a quick increase of the pycnocline water density which entrains rapidly salty water [see the time interval before point *G* in Figs. 6(b), 6(c), and 7(c)]. In a first phase, the gravity current flow moves upward over the sloped boundary, intruding into the intermediate density layer, whose mean density increases [see the time interval between points *G* and *H* in Figs. 6(b), 6(c), and 7(c)]. As it propagates over the sloped boundary and approaches the free surface, the gravity current decelerates and interacts with the upper layer containing fresh water [case 3 in Fig. 5(j)]. As this happens, a decrease of the pycnocline water mean density due to entrainment of fresh water is observed [see the time interval after point *H* in Figs. 6(b), 6(c), and 7(c)], which is similar to what was observed in the collapsing case. Later on, the entrainment of salty water remains roughly unchanged, while the entrainment of fresh water increases with time.

This is probably due to the horizontal rearrangement of the pycnocline water towards a more stable hydrostatic condition.

V. POTENTIAL ENERGY AND IRREVERSIBLE MIXING

Mixing within a breaking ISW is herein quantified by the energy budget method of Winters *et al.* [69], which has been widely used in the literature (see, e.g., [50,67,70,71]). This method does not consider the change in the volume of the pycnocline water; thus it is not required to define any isodensity interface. Considering the density field $\rho(x, y, z, t)$ for a closed system, where x, y, and z are the streamwise, vertical, and spanwise coordinates, respectively, mixing of the density field corresponds to a change in the probability density function (PDF) of the density induced by mass diffusion. This change results in a reduction of the density variance. Turbulence enhances the blending of fluid parcels by steepening scalar gradients and increasing isoscalar surfaces, the regions along which diffusion develops [72]. In the energy budget method, diabatic and adiabatic processes are distinguished. An adiabatic process can change the potential energy of the fluid by switching the kinetic energy into potential energy without inducing any diffusive mixing (i.e., no heat or mass transfer occurs). The diabatic processes properly quantify the energetics of mixing. They are responsible for the change of the total potential energy of the fluid due to irreversible molecular diffusion. In order to distinguish between the contribution of diabatic and adiabatic processes, the concepts of background and available potential energy have to be introduced [69]. The volume-integrated kinetic energy and the gravitational potential energy of the flow are defined as

$$E_k(t) = \frac{\rho_0}{2}\int_V (u^2 + v^2 + w^2)dV, \tag{9}$$

$$E_p(t) = g\int_V \rho(x, y, z, t)y\,dV, \tag{10}$$

where ρ_0 is a constant reference density; u, v, and w are the streamwise, vertical, and spanwise velocity components respectively; $\rho(x, y, z, t)$ is the local instantaneous density field; and V is the entire volume of the domain. The instantaneous volume-integrated background potential energy is defined as

$$E_b(t) = g\int_V \tilde{\rho}(x, y, z, t)y\,dV, \tag{11}$$

where $\tilde{\rho}(x, y, z, t)$ represents the density field in the configuration of the minimum potential energy obtained by sorting the fluid parcels by an adiabatic volume-conserving rearrangement. The background potential energy is uniquely defined by the PDF of density and thus is independent of the instantaneous spatial distribution of density in the flow domain. The difference between the total energy and the background potential energy defines the volume-integrated available potential energy

$$E_a(t) = E_p(t) - E_b(t). \tag{12}$$

The available potential energy quantifies the amount of potential energy released in the adiabatic transition from $\rho(x, y, z, t)$ to $\tilde{\rho}(x, y, z, t)$ without altering the PDF of density. It is the amount of potential energy stored in the fluid when it is not in gravitational equilibrium [73]. Changes in the background potential energy are thus associated with the energy consumed in mixing the fluid and can be used to characterize this process.

The energy budget was evaluated for all cases. Qualitatively, the temporal variations of the kinetic energy, total background potential energy, and available potential energy terms were similar in these cases. For brevity, only results for the collapsing case are presented in Fig. 8(a). When plotted, the energy variables E have the initial value E_0 removed. The dimensional variables are then normalized by the absolute value of the minimum available potential energy $|E_{a,\min}|$. The energy that is no

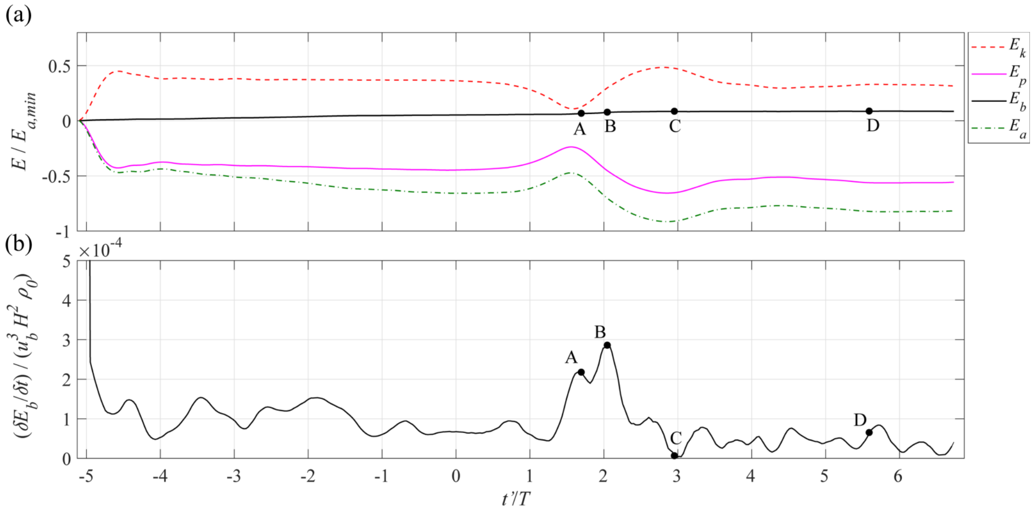

FIG. 8. (a) Temporal variation of volume-integrated energy for the collapsing case. The kinetic energy E_k, total potential energy E_p, background potential energy E_b, and available potential energy E_a are all normalized by $|E_{a,\min}|$. (b) Normalized rate of change of background potential energy for the collapsing case. Points A–D are defined in Fig. 3.

longer available due to irreversible mixing can be evaluated by calculating the change in background potential energy between consecutive states of the system. Figure 8(b) shows the rate of change of the nondimensional background potential energy for the collapsing case.

As the wave starts to experience the presence of the sloping boundary, its celerity decreases. As a result, the volume-integrated kinetic energy inside the domain starts decaying. As this happens, the ISW is modifying its shape and the lighter fluid parcels tend to move downward [Fig. 3(a)]. For this reason, both the total and the available potential energies increase, while remaining equal to each other. The background potential energy is thus equal to zero. The kinetic energy starts to increase during the breaking event. The motion induced by the boundary layer separation [Fig. 3(b)] uplifts the lighter water parcel and induces mixing. The time evolution of the background potential energy shows the presence of a first peak during the time interval the bolus forms and of a second, more pronounced, peak during the time period when the whirling motion causes mixing [points A and B, respectively, in Fig. 8(b)]. As the counterclockwise vortex loses its coherence, the rate of change of E_b decreases. This lasts until the formation of the gravity current [point C in Fig. 8(b)]. The fluid motion inside the domain is now characterized by the presence of a gravity current flowing upslope and a reflected wave moving offshore. For these reasons, the kinetic energy and the potential energy assume their maximum and minimum values, respectively. When the gravity current flows upslope it induces mixing, which in turn results in slight variations of the background potential energy. In particular, when the gravity current reaches its highest position over the sloping boundary [Fig. 3(e)], a more pronounced variation of E_b is observed [point C in Fig. 8(b)].

The rate of change of the background potential energy is not a direct measure of the amount of mixing. Rather the mixing efficiency is used to quantify mixing, by evaluating the relation between the change in PDF and the system energetics. In a stratified flow, the mixing efficiency quantifies the fraction of energy consumed by irreversible diabatic mixing related to the amount of energy available to support this process (i.e., the mechanical energy). As widely used in previous experimental and computational studies (see, e.g., [74–77]), the instantaneous mixing efficiency is defined as

$$\eta = \frac{\Delta E_b}{|\Delta E_T|}, \tag{13}$$

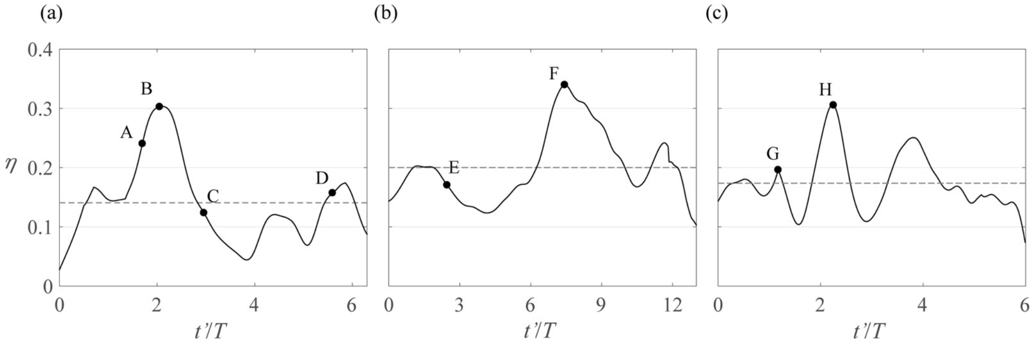

FIG. 9. Instantaneous mixing efficiency η and bulk mixing efficiency η_m (dashed lines) for (a) the collapsing case, (b) the plunging case, and (c) the surging case. Points A–H are defined in Figs. 3 and 5.

where Δ is the change between two consecutive states of the system and E_T is the instantaneous total mechanical energy of the fluid

$$E_T(t) = E_a(t) + E_k(t). \tag{14}$$

Figure 9 shows the temporal variation of the mixing efficiency in the three cases and its mean value during the corresponding breaker event. For the collapsing case, as the wave approaches the incline, it decelerates and consequently partially dissipates. The first peak of the mixing efficiency is observed for $t'/T < 1$ [Fig. 9(a)] as the volume-integrated kinetic energy starts to decrease [Fig. 8(a)]. Then, as the wave interacts with the sloping boundary, the changes in wave geometric and kinematic features cause an approximately linear increase of the mixing efficiency with time. Its maximum value is recorded during the dissipation of the counterclockwise vortex induced by the boundary layer separation [point B in Fig. 9(a)]. During the upslope propagation of the gravity current, the value of η increases in an irregular way. Three peaks of increasing magnitude are observed during the time interval between point C and point D [Fig. 9(a)]. During this phase, the mixing peaks when the gravity current reaches the upper layer close to the free surface [point D in Fig. 8(a)]. Because of the interaction between the gravity current and the surrounding lighter fluid, mixing is strong, which explains the peak in the mixing efficiency at point D.

In the plunging case [Fig. 9(b)], the clockwise vortex induced by the overturning of the rear edge of the wave causes the entrainment of a large amount of salty water for $0 < t'/T < 2.5$ [point E in Fig. 7(b)]. The mixing efficiency then decreases before starting to increase again for $t'/T > 4$ and it peaks around $t'/T = 7.5$ [point F in Fig. 9(b)]. During this phase, the formation of the gravity current is observed. As the gravity current flows upslope, it entrains lighter fluid [Fig. 7(b)], which causes mixing. For the same reason explained in the collapsing case, when the gravity current reaches the upper layer close to the free surface, the mixing and mixing efficiency peak again [$t'/T = 11.5$ in Fig. 9(b)].

The instantaneous mixing efficiency for the surging case contains four peaks [Fig. 9(c)]. The first one occurs for $t'/T = 0.8$, as the wave interacts with the sloping boundary, which induces strong dissipation. As the wave trough reaches its lowest position over the incline, small instabilities develop due to boundary layer separation. A peak of the mixing efficiency occurs at this time [point G in Fig. 9(c)]. The breaking event continues with the formation of a gravity current flowing upslope that induces strong local mixing. The peak of the mixing efficiency is reached when the gravity current reaches its highest position over the sloped boundary [point H in Fig. 9(c)]. Around $t'/T = 4$, a third peak of the mixing efficiency is observed. This peak is probably due to the horizontal rearrangement of the intermediate density layer towards a stable hydrostatic condition. Our results are in agreement in terms of bulk mixing efficiency and mixing efficiency peaks with the values obtained by Arthur and Fringer [45].

VI. CONCLUSION

Using high-resolution numerical simulations, we reproduced three laboratory experiments of internal solitary waves interacting with a sloping boundary. The numerical approach allowed us to analyze and quantify three different types of breaking events by linking the different instabilities and dynamics of each type of breaker wave with the temporal evolution of the density fields. For the plunging breaker case, an instability develops as the wave experiences the presence of the sloping boundary in the form of a clockwise vortex induced by the overturning of the trailing edge of the wave. Compared to the other cases, this instability occurs in the internal part of the flow beneath the wave, relatively far from the bottom. Immediately after the edge overturning, a large amount of salty water runs over the wave, which results in strong salty water entrainment into the pycnocline water. The instantaneous mixing efficiency increases rapidly to 0.2, as the wave starts interacting with the sloping boundary and then remains approximately constant until the turbulent structure dissipates. During these times ($t'/T = 1$–2), the thin layer of salty water is pushed down the incline by the approaching wave, which induces a large amplification of the bed shear stress. The instability characterizing the plunging breaker causes initially a large entrainment into the pycnocline region, while the mixing efficiency peaks only at a later stage as the mixed region reaches the sloping boundary. A relatively large time delay occurring between the two processes is observed.

In the collapsing breaker case, the heavier fluid is forced to accelerate downward in the vicinity of the sloped boundary, before the wave trough reaches the sloping surface. The consequent boundary layer separation generates a fresh water bolus characterized by a counterclockwise motion that induces strong entrainment of salty water into the intermediate density layer. The vortex dissipation occurs rapidly, thus entrainment and mixing occur in quick succession: The maximum mixing efficiency is observed after the bolus generated by boundary layer separation forms. After the bolus dissipates, a gravity current is generated by the unstable density distribution over the sloping boundary. The gravity current flows upslope, inducing entrainment of fresh water into the pycnocline water. During this phase, the entrainment increases linearly while the mixing efficiency shows several peaks of increasing values. This is probably due to the formation of successive Kelvin-Helmholtz billows at the interface.

In the surging case, the entire breaking event is very similar to the one observed for the collapsing breaker case. The main difference between the two cases can be found in the energetics of the boundary layer separation. Because a larger Iribarren number is needed for a surging breaker to occur, the sloping boundary should have a minimum inclination with respect to the wave slope. As the wave approaches the slope, the downstream deceleration of the heavier fluid over the incline in the adverse pressure gradient region causes boundary layer separation. Consequently, the formation of a small bolus occurs. Because the ISW generated is bigger (i.e., faster) than the one generated in case 1 (the collapsing breaker case), one could expect stronger instabilities to develop for the surging breaker case. Nevertheless, a comparison of both the bolus size in Figs. 3(b) and 5(g) and the mixing efficiency in Figs. 9(a) (point B) and 9(c) (point G) proves that this instability is less energetic for the surging breaker. As a result, the gravity current moving upward over the sloping boundary is bigger and more energetic in the surging breaker case [Fig. 5(i)] compared to the one in the collapsing breaker case [Fig. 3(d)].

Although the maximum entrainment values are very different in the three cases, the bulk mixing efficiency values during the breaking event are similar. The maximum amount of entrainment is observed in the surging breaker case whereas the difference with the other two cases is not very significant. Thus, the surging breaker case is characterized by a lower mixing compared to the other two cases.

The entrainment parameter and the mixing efficiency represent different indicators of the effects of turbulent instabilities. Nevertheless, they should both be taken into account for a clear and complete description of mixing occurring within a stratified fluid system. Changes in the intermediate water entrainment parameter are associated with the rate of decrease of water volumes with constant density values (i.e., the uniform upper and lower layers). Moreover, mixing processes involve the generation of a mixed region characterized by more uniform properties. Thus, changes of the density profile, evaluated in the state of minimum potential energy, can be completely described by considering both entrainment (which influences the thickness of the density profile with intermediate density values) and mixing (which affects the density profile within the mixed region). With respect to other ISW breaking mechanisms, the results reported in the present paper show that a plunging breaker is expected to induce changes of the initial density profile, by increasing both the region characterized by intermediate values and the vertical displacement between the inflection points.

[1] C. Garrett, Internal tides and ocean mixing, Science **301**, 1858 (2003).

[2] J. Pedlowsky and J. W. Miles, Waves in the ocean and atmosphere: Introduction to wave dynamics, Appl. Mech. Rev. **57**, B20 (2004).

[3] J. Grue, A. Jensen, P.-O. Rusås, and J. K. Sveen, Breaking and broadening of internal solitary waves, J. Fluid Mech. **413**, 181 (2000).

[4] M. Bakhoday-Paskyabi, Particle motions beneath irrotational water waves, Ocean Dyn. **65**, 1063 (2015).

[5] K. G. Lamb, Particle transport by nonbreaking, solitary internal waves, J. Geophys. Res.: Oceans **102**, 18641 (1997).

[6] J. J. Leichter, S. R. Wing, S. L. Miller, and M. W. Denny, Pulsed delivery of subthermocline water to Conch Reef (Florida Keys) by internal tidal bores, Limnol. Oceanogr. **41**, 1490 (1996).

[7] K. A. Davis and S. G. Monismith, The modification of bottom boundary layer turbulence and mixing by internal waves shoaling on a barrier reef, J. Phys. Oceanogr. **41**, 2223 (2011).

[8] R. K. Walter, C. B. Woodson, R. S. Arthur, O. B. Fringer, and S. G. Monismith, Nearshore internal bores and turbulent mixing in southern Monterey Bay, J. Geophys. Res. **117**, C07017 (2012).

[9] M. M. Omand, J. J. Leichter, P. J. S. Franks, R. T. Guza, A. J. Lucas, and F. Feddersen, Physical and biological processes underlying the sudden surface appearance of a red tide in the nearshore, Limnol. Oceanogr. **56**, 787 (2011).

[10] R. K. Walter, C. B. Woodson, P. R. Leary, and S. G. Monismith, Connecting wind-driven upwelling and offshore stratification to nearshore internal bores and oxygen variability, J. Geophys. Res.: Oceans **119**, 3517 (2014).

[11] D. Bogucki, T. Dickey, and L. G. Redekopp, Sediment resuspension and mixing by resonantly generated internal solitary waves, J. Phys. Oceanogr. **27**, 1181 (1997).

[12] J. M. Klymak and J. N. Moum, Internal solitary waves of elevation advancing on a shoaling shelf, Geophys. Res. Lett. **30**, 2045 (2003).

[13] P. Hosegood, J. Bonnin, and H. van Haren, Solibore-induced sediment resuspension in the Faeroe-Shetland Channel, Geophys. Res. Lett. **31**, L09301 (2004).

[14] P. Hosegood and H. van Haren, Near-bed solibores over the continental slope in the Faeroe-Shetland Channel, Deep-Sea Res. Pt. II **51**, 2943 (2004).

[15] G. S. Carter, M. C. Gregg, and R.-C. Lien, Internal waves, solitary-like waves, and mixing on the Monterey Bay Shelf, Cont. Shelf Res. **25**, 1499 (2005).

[16] L. S. Quaresma, J. Vitorino, A. Oliveira, and J. da Silva, Evidence of sediment resuspension by nonlinear internal waves on the western portuguese mid-shelf, Mar. Geol. **246**, 123 (2007).

[17] R. Droghei, F. Falcini, D. Casalbore, E. Martorelli, R. Mosetti, G. Sannino, R. Santoleri, and F. L. Chiocci, The role of internal solitary waves on deep-water sedimentary processes: The case of up-slope migrating sediment waves off the Messina Strait, Sci. Rep. **6**, 36376 (2016).

[18] D. J. Korteweg and G. De Vries, XLI. On the change of form of long waves advancing in a rectangular canal, and on a new type of long stationary waves, Philos. Mag. **39**, 422 (1895).

[19] W. Alpers and E. Salusti, Scylla and Charybdis observed from space, J. Geophys. Res.: Oceans **88**, 1800 (1983).

[20] W. Alpers, P. Brandt, A. Rubino, and J. O. Backhaus, Recent contributions of remote sensing to the study of internal waves in the straits of Gibraltar and Messina, Bull. Inst. Oceanogr. **17**, 21 (1996).

[21] V. Artale, D. Levi, S. Marullo, and R. Santoleri, Analysis of nonlinear internal waves observed by landsat thematic mapper, J. Geophys. Res.: Oceans **95**, 16065 (1990).

[22] P. Brandt, A. Rubino, D. Quadfasel, W. Alpers, J. Sellschopp, and H.-V. Fiekas, Evidence for the influence of Atlantic-Ionian stream fluctuations on the tidally induced internal dynamics in the Strait of Messina, J. Phys. Oceanogr. **29**, 1071 (1999).

[23] A. Scotti and J. Pineda, Observation of very large and steep internal waves of elevation near the Massachusetts coast, Geophys. Res. Lett. **31**, L22307 (2004).

[24] K. Nakayama, T. Shintani, K. Kokubo, T. Kakinuma, Y. Maruya, K. Komai, and T. Okada, Residual currents over a uniform slope due to breaking of internal waves in a two-layer system, J. Geophys. Res.: Oceans **117**, C10002 (2012).

[25] D. Bourgault, M. Morsilli, C. Richards, U. Neumeier, and D. E. Kelley, Sediment resuspension and nepheloid layers induced by long internal solitary waves shoaling orthogonally on uniform slopes, Cont. Shelf Res. **72**, 21 (2014).

[26] R. S. Arthur and O. B. Fringer, Transport by breaking internal gravity waves on slopes, J. Fluid Mech. **789**, 93 (2016).

[27] T. W. Kao, F.-S. Pan, and D. Renouard, Internal solitons on the pycnocline: Generation, propagation, and shoaling and breaking over a slope, J. Fluid Mech. **159**, 19 (1985).

[28] K. R. Helfrich, Internal solitary wave breaking and run-up on a uniform slope, J. Fluid Mech. **243**, 133 (1992).

[29] H. Michallet and G. N. Ivey, Experiments on mixing due to internal solitary waves breaking on uniform slopes, J. Geophys. Res.: Oceans **104**, 13467 (1999).

[30] L. Boegman, G. N. Ivey, and J. Imberger, The degeneration of internal waves in lakes with sloping topography, Limnol. Oceanogr. **50**, 1620 (2005).

[31] G. La Forgia, C. Adduce, and F. Falcini, Laboratory investigation on internal solitary waves interacting with a uniform slope, Adv. Water Resour. **120**, 4 (2018).

[32] K. Nakayama and J. Imberger, Residual circulation due to internal waves shoaling on a slope, Limnol. Oceanogr. **55**, 1009 (2010).

[33] V. Lombardi, C. Adduce, G. Sciortino, and M. L. Rocca, Gravity currents flowing upslope: Laboratory experiments and shallow water simulations, Phys. Fluids **27**, 016602 (2015).

[34] E. McPhee-Shaw, Boundary-interior exchange: Reviewing the idea that internal-wave mixing enhances lateral dispersal near continental margins, Deep-Sea Res. Pt. II **53**, 42 (2006).

[35] Z. Borden, E. Meiburg, and G. Constantinescu, Internal bores: An improved model via a detailed analysis of the energy budget, J. Fluid Mech. **703**, 279 (2012).

[36] Z. Borden, T. Koblitz, and E. Meiburg, Turbulent mixing and wave radiation in non-Boussinesq internal bores, Phys. Fluids **24**, 082106 (2012).

[37] K. G. Lamb, A numerical investigation of solitary internal waves with trapped cores formed via shoaling, J. Fluid Mech. **451**, 109 (2002).

[38] D. Bourgault, M. D. Blokhina, R. Mirshak, and D. E. Kelley, Evolution of a shoaling internal solitary wavetrain, Geophys. Res. Lett. **34**, L03601 (2007).

[39] V. Vlasenko and N. Stashchuk, Three-dimensional shoaling of large-amplitude internal waves, J. Geophys. Res.: Oceans **112**, C11018 (2007).

[40] V. Vlasenko and K. Hutter, Numerical experiments on the breaking of solitary internal wavesover a slope-shelf topography, J. Phys. Oceanogr. **32**, 1779 (2002).

[41] S. K. Venayagamoorthy and O. Fringer, Numerical simulations of the interaction of internal waves with a shelf break, Phys. Fluids **18**, 076603 (2006).

[42] S. K. Venayagamoorthy and O. B. Fringer, On the formation and propagation of nonlinear internal boluses across a shelf break, J. Fluid Mech. **577**, 137 (2007).

[43] P. Aghsaee, L. Boegman, and K. G. Lamb, Breaking of shoaling internal solitary waves, J. Fluid Mech. **659**, 289 (2010).

[44] B. Gayen and S. Sarkar, Turbulence During the Generation of Internal Tide on a Critical Slope, Phys. Rev. Lett. **104**, 218502 (2010).

[45] R. S. Arthur and O. B. Fringer, The dynamics of breaking internal solitary waves on slopes, J. Fluid Mech. **761**, 360 (2014).

[46] B. Gayen and S. Sarkar, Boundary mixing by density overturns in an internal tidal beam, Geophys. Res. Lett. **38**, L14608 (2011).

[47] B. R. Sutherland and K. J. Ivey, Shoaling internal solitary waves, J. Geophys. Res. Ocean **118**, 4111 (2013).

[48] C. Cenedese and C. Adduce, Mixing in a density-driven current flowing down a slope in a rotating fluid, J. Fluid Mech. **604**, 369 (2008).

[49] H. I. S. Nogueira, C. Adduce, E. Alves, and M. J. Franca, Dynamics of the head of gravity currents, Environ. Fluid Mech. **14**, 519 (2014).

[50] L. Ottolenghi, C. Adduce, R. Inghilesi, V. Armenio, and F. Roman, Entrainment and mixing in unsteady gravity currents, J. Hydraul. Res. **54**, 541 (2016).

[51] L. Ottolenghi, C. Adduce, F. Roman, and V. Armenio, Analysis of the flow in gravity currents propagating up a slope, Ocean Model. **115**, 1 (2017).

[52] L. Ottolenghi, P. Prestininzi, A. Montessori, C. Adduce, and M. La Rocca, Lattice Boltzmann simulations of gravity currents, Eur. J. Mech. B **67**, 125 (2017).

[53] C.-Y. Chen, J. R.-C. Hsu, C.-W. Chen, H.-H. Chen, C.-F. Kuo, and M.-H. Cheng, Generation of internal solitary wave by gravity collapse, J. Mar. Sci. Technol. **15**, 1 (2007).

[54] S. K. Ooi, G. Constantinescu, and L. Weber, A numerical study of intrusive compositional gravity currents, Phys. Fluids **19**, 076602 (2007).

[55] T. Tokyay, G. Constantinescu, and E. Meiburg, Lock-exchange gravity currents with a high volume of release propagating over a periodic array of obstacles, J. Fluid Mech. **672**, 570 (2011).

[56] T. Tokyay, G. Constantinescu, and E. Meiburg, Tail structure and bed friction velocity distribution of gravity currents propagating over an array of obstacles, J. Fluid Mech. **694**, 252 (2012).

[57] T. Tokyay, G. Constantinescu, and E. Meiburg, Lock-exchange gravity currents with a low volume of release propagating over an array of obstacles, J. Geophys. Res.: Oceans **119**, 2752 (2014).

[58] C. D. Pierce and P. Moin, *Progress-Variable Approach for Large-Eddy Simulation of Turbulent Combustion* (Stanford University Press, Stanford, 2001).

[59] W. Rodi, G. Constantinescu, and T. Stoesser, *Large-Eddy Simulation in Hydraulics* (CRC, Boca Raton, 2013).

[60] T. Tokyay and G. Constantinescu, The effects of a submerged non-erodible triangular obstacle on bottom propagating gravity currents, Phys. Fluids **27**, 056601 (2015).

[61] K. Steenhauer, T. Tokyay, and G. Constantinescu, Dynamics and structure of planar gravity currents propagating down an inclined surface, Phys. Fluids **29**, 036604 (2017).

[62] T. Sommer, F. Danza, J. Berg, A. Sengupta, G. Constantinescu, T. Tokyay, H. Bürgmann, Y. Dressler, O. Sepúlveda Steiner, C. J. Schubert, M. Tonolla, and A. Wüest, Bacteria-induced mixing in natural waters, Geophys. Res. Lett. **44**, 9424 (2017).

[63] S. K. Ooi, G. Constantinescu, and L. Weber, Numerical simulations of lock-exchange compositional gravity current, J. Fluid Mech. **635**, 361 (2009).

[64] F. Necker, C. Härtel, L. Kleiser, and E. Meiburg, Mixing and dissipation in particle-driven gravity currents, J. Fluid Mech. **545**, 339 (2005).

[65] M. I. Cantero, J. R. Lee, S. Balachandar, and M. H. Garcia, On the front velocity of gravity currents, J. Fluid Mech. **586**, 1 (2007).

[66] C. Adduce, G. Sciortino, and S. Proietti, Gravity currents produced by lock exchanges: Experiments and simulations with a two-layer shallow-water model with entrainment, J. Hydraul. Eng.-ASCE **138**, 111 (2012).

[67] L. Ottolenghi, C. Adduce, R. Inghilesi, F. Roman, and V. Armenio, Mixing in lock-release gravity currents propagating up a slope, Phys. Fluids **28**, 056604 (2016).

[68] L. Ottolenghi, C. Cenedese, and C. Adduce, Entrainment in a dense current flowing down a rough sloping bottom in a rotating fluid, J. Phys. Oceanogr. **47**, 485 (2017).

[69] K. B. Winters, P. N. Lombard, J. J. Riley, and E. A. D'Asaro, Available potential energy and mixing in density-stratified fluids, J. Fluid Mech. **289**, 115 (1995).

[70] A. T. Fragoso, M. D. Patterson, and J. S. J. S. Wettlaufer, Mixing in gravity currents, J. Fluid Mech. **734**, R2 (2013).

[71] M. D. Patterson, C. P. Caulfield, J. N. McElwaine, and S. B. Dalziel, Time-dependent mixing in stratified Kelvin-Helmholtz billows: Experimental observations, Geophys. Res. Lett. **33**, L15608 (2006).

[72] K. B. Winters and E. A. D'Asaro, Diascalar flux and the rate of fluid mixing, J. Fluid Mech. **317**, 179 (1996).

[73] E. N. Lorenz, Available potential energy and the maintenance of the general circulation, Tellus **7**, 157 (1955).

[74] G. N. Ivey and J. Imberger, On the nature of turbulence in a stratified fluid. Part I: The energetics of mixing, J. Phys. Oceanogr. **21**, 650 (1991).

[75] W. R. Peltier and C. P. Caulfield, Mixing efficiency in stratified shear flows, Annu. Rev. Fluid Mech. **35**, 135 (2003).

[76] S. B. Dalziel, M. D. Patterson, C. P. Caulfield, and I. A. Coomaraswamy, Mixing efficiency in high-aspect-ratio Rayleigh-Taylor experiments, Phys. Fluids **20**, 065106 (2008).

[77] T. Prastowo, R. W. Griffiths, G. O. Hughes, and A. M. Hogg, Effects of topography on the cumulative mixing efficiency in exchange flows, J. Geophys. Res.: Oceans **114**, C08008 (2009).